

ARTICLE

Experimental investigations on the shear strength of prestressed beam elements with a focus on the analysis of crack kinematics

Sebastian Thoma  | Oliver Fischer

Chair of Concrete and Masonry Structures, Technical University of Munich, Munich, Germany

Correspondence

Sebastian Thoma, TUM, Theresienstraße 90, 80333 Munich, Germany.
Email: sebastian.thoma@tum.de

Funding information

Federal Highway Research Institute of Germany

Abstract

The shear strength of prestressed concrete girders with a low amount of web reinforcement is an ongoing subject of research, in particular with regard to the assessment of existing concrete bridges. In this paper, a series of experiments is presented that addresses this question and at the same time significantly lowers the degree of longitudinal reinforcement in line with efficiently designed bridge cross-sections and contrary to the vast majority of representative scaled test series. The limit case observations allow for a shear failure of the system even in the case of yielding longitudinal reinforcement due to the incremental strain in the tendons that could be activated. The focus of the presented analysis lies within the load-dependent crack kinematics of the beam elements on the basis of the digital image correlation. It is shown that, depending on the longitudinal strain of the cross-section, load-bearing components associated with aggregate interlock do not seem to be mechanically reasonable and an extent of plasticity-theoretical ideas through a compression chord component appears to be more consistent.

KEYWORDS

continuous beams, crack kinematics, plasticity theory, shear strength

NOTATIONS

α_{cc} factor to take into account long-term effects on compressive strength and to convert between cylindrical compressive strength and unconfined compressive strength of concrete

$\Delta\sigma_p$	stress increase of tendons
$\delta_{n,t}$	local crack opening and sliding deformations
η_{fc}	reduction factor accounting for brittleness of concrete
$\gamma_{i,j}$	difference angles for deriving the local fracture mode
γ_{xy}	shear strain
ν	median
ω	mechanical longitudinal reinforcement ratio
ρ_{sl}	longitudinal reinforcement ratio
σ	standard deviation

Discussion on this paper must be submitted within two months of the print publication. The discussion will then be published in print, along with the authors' closure, if any, approximately nine months after the print publication.

This is an open access article under the terms of the [Creative Commons Attribution-NonCommercial-NoDerivs](https://creativecommons.org/licenses/by-nc-nd/4.0/) License, which permits use and distribution in any medium, provided the original work is properly cited, the use is non-commercial and no modifications or adaptations are made.

© 2023 The Authors. Structural Concrete published by John Wiley & Sons Ltd on behalf of International Federation for Structural Concrete

σ_c	compressive stress in concrete
σ_{cp}	normal compressive stress in concrete due to the horizontal component of prestressing
$\sigma_{n,t}$	local stress components along crack contours
$\sigma_{sl,i}$	stress in longitudinal reinforcement due to external loading
θ	compression strut angle
ϵ_1	principle tensile strain
ϵ_{c1}	concrete compressive strain at maximum load
ϵ_{c2}	concrete compressive strain at crushing
ϵ_{xm}	mean longitudinal strain
$\epsilon_{y,sw}$	yield strain of stirrups
ϵ_z	strain in concrete parallel to stirrups
\emptyset	diameter of reinforcing bars, equivalent diameter of strands
c	traced normal vector from crack contours
r	displacement vector resulting from DIC data
A_{10}	fracture strain
A_c	cross-sectional area of beam elements
a_d	dilatancy ratio
A_{gt}	uniform strain without necking of steel probe
A_p	cross-sectional area of prestressed tendons
A_{sl}	cross-sectional area of nonprestressed longitudinal reinforcement
$b_{w,nom}$	effective web width
d	effective cross-section depth
DIC	digital image correlation
E_{cm}	secant modulus of concrete
E_{ii}	Langrange distortion
$E_{s/p}$	secant modulus of reinforcing steel/ prestressed strands
F	field moment area
$f_{c,cyl}$	cylinder compressive strength of concrete
$f_{ct,sp}$	tensile splitting strength of concrete
f_{Rm}	related rib area of reinforcing bars
f_{Rnorm}	related rib area of reinforcing bars required by standard
k_c	reduction factor for concrete compressive strength due to transverse tensile strain
PR	Parabola-Rectangle graph of concrete under compression
R_m	tensile strength of reinforcing steel/ prestressed strands
$R_{s/p,0.2}$	offset yield strength at 0.2% strain of reinforcing steel/ prestressed strands
S	support moment area
V_{max}	shear resistance
$V_{p,v}$	shear resistance of inclined tendons (vertical component)
$V_{r,c}$	compression strut capacity
V_{sw}	shear resistance of stirrups
VSG	virtual strain gauge
x_c	compression zone height

x_{gap}	joint opening from external load at the shear key profiling, initial precompressed tension zone
z	inner lever arm

1 | INTRODUCTION

For the evaluation of existing bridges and especially in the light of specific questions on prestressed concrete bridge construction, theoretical and experimental efforts for the assessment of the shear strength capacity have been intensified in the recent past, as in particular characteristic load-bearing mechanisms of prestressed continuous beams with a low amount of shear reinforcement are continuously under discussion.^{1–6} A feature that is largely common to previous experimental investigations is found in the comparatively high degree of longitudinal reinforcement of the test specimens, which should avoid premature bending failure in favor of the desired shear failure. Individual test series on the influence of the degree of longitudinal reinforcement or the strain state of the longitudinal reinforcement in connection with the shear behavior of reinforced concrete beams suggest that an oversized longitudinal reinforcement implicitly influences the shear transfer actions and thus possibly falsifies the transferability of experimental evidence to economically designed bridge girders.^{7–9} The influence of yielding longitudinal reinforcement, associated beam rotation and its effect on the shear capacity of nonprestressed beam systems are discussed in detail in.¹⁰ Again, the significant deformations of the chords show a negative influence on achievable shear capacities, which can be attributed to the reduced concrete load-bearing component. A consideration of the influence of the strain state in the case of mixed reinforced tension chords including conventional reinforcement and post-tensioned tendons is investigated for the first time within the scope of the presented experiments. Given this background, a test series of rectangular and T-beam cross-sections was conducted to investigate the shear capacity and fracture behavior with successively reduced longitudinal reinforcement levels. An essential observation is that -despite plastic deformation of the tension chord reinforcement for the lowest but still practical plausible degree of longitudinal reinforcement-the ultimate load capacity is governed by a shear failure of the system with a corresponding increase in strain in the tendons, which upholds the internal equilibrium.

After presenting the experimental programme and the underlying boundary conditions and results (chapter 2), chapter 3 discuss a possible integration of the gained insights into the assumptions of the theory of plasticity. The capacity of the concrete web, excluding a concrete compression failure and the vertical component of inclined

tendons as part of the shear strength, is defined according to the plasticity theory by the exploitation of the web reinforcement using a compression strut angle θ , which describes the lower-bound solution.¹¹ However, the range of shear force tests carried out on prestressed beam elements demonstrates in a unified manner that further, far more dominant load-bearing components are effective and thus an extension in the consideration of classical resisting mechanisms is required to capture those effects and make a more precise assessment of the shear strength to be expected. There are already various empirically or mechanically analytical approaches to this.^{2,5,6,12–14} Accompanying thoughts on the description of an additional concrete transfer action component are tackled in this paper in such a way that basic mechanical thoughts on the phenomenological description of the shear cracking behavior are discussed on the basis of processed evaluations of the digital image correlation (DIC). The DIC analysis allows continuous, full-surface evaluation of the crack formation progress and resulting kinematics.^{15,16} This can be a contribution in the validation and weighting of individual vacant load-bearing components, especially with regard to the option of crack-bridging stresses. Chapter 4 describes the knowledge gained from digital image correlation and the selected approaches for evaluation. On the basis of the results, existing model concepts, as briefly discussed in chapter 5, can be delimited and key points for further analyses can be defined.

2 | EXPERIMENTS

2.1 | Test setup

Instead of conventional continuous beam systems, prestressed beam elements, so-called substructures, are tested in a test setup specially designed for this purpose at the institute,^{1,17} while the basic idea for testing extracted substructures has already been used successfully before, for example, ref. 18. The analysis of the shear behavior focuses on the region between the load introduction and the central support of a reference continuous beam, cf. (Figure 1a). This domain is considered in a isolated manner, taking into account the applied internal forces and the compatibility of the deformations and rotations in the exposed edge of the section. Analogous to the reference system, a linear bending moment curve with a constant shear force is obtained along the beam element. The shear slenderness of the tested systems is therefore $\lambda \approx 3$, which suggests a primary and also desired beam action under shear while the influence of direct compression struts appears negligible.¹⁹ Including the mixed reinforced tension chord (incl. tendons) and the resulting weighted static effective height reduces this reference value, as does the degree of prestressing, which

influences the geometric stiffness. The load introducing plate, shown on the left in Figure 1, applies the load via six individually controllable axes (two cylinders each in position and orientation in the depth of the illustration). In addition to the two vertical cylinders, which are mainly responsible for the vertical load vector, the two horizontal pairs of cylinders ensure the positive span moment. Forces and moments result from a matrix-vector product of known cylinder forces, movements and fixed point coordinates when transformed around a global system pole. The displacement of the fixed point coordinates of the cylinders as a result of elastic deformation of the retaining structures are also measured and compensated for in the control system. The right load plate receives the forces, but subsequent reaction bars are rigid truss bars without integration into the control system. The shear key profile serves to transfer the shear force. The compression zone is designed as a dry joint contact on both sides, while the reinforcement in the corresponding tension chord and the tendons are each anchored at the back of the rigid load plates. Further information and illustrative figures on the application of the substructure technique can be found here.²⁰

2.2 | Test program

The test series considers the influence of a gradually reduced degree of longitudinal reinforcement on rectangular cross-sections and T-beams. All beam elements provide a very small amount of shear reinforcement, which corresponds to about 90% of the minimum shear reinforcement according to Eurocode 2.²¹ The further structural detailing of the design remains unchanged, cf. (Figure 1c). Material parameters were determined on the day a beam element test was carried out, 28 days after casting at the earliest. For workability reasons, a concrete with a maximum aggregate size of 8 mm without additives was chosen. The main material parameters, the varying degree of longitudinal reinforcement, chosen prestressing (compressive normal stress in the concrete in height of the gravity axis in the middle of the beam element) and achieved failure loads are summarized in Tables 1 and 2. The selected design leads to initial prestressing steel stresses of approx. 600–700 MPa, which represent a comparatively low utilization of the prestressing steel. This approach was chosen in order to adequately connect to the data basis of the tests of previous projects.^{1,22} To establish the post-tensioning bond, the tendons, which are routed in flat ducts, are then grouted with mortar. The grout achieved a compressive strength of 68.0 MPa and a tensile strength of 6.2 MPa at the prism on average in all tests. The first letter of the test ID indicates the cross-section type, the numbering reflects the

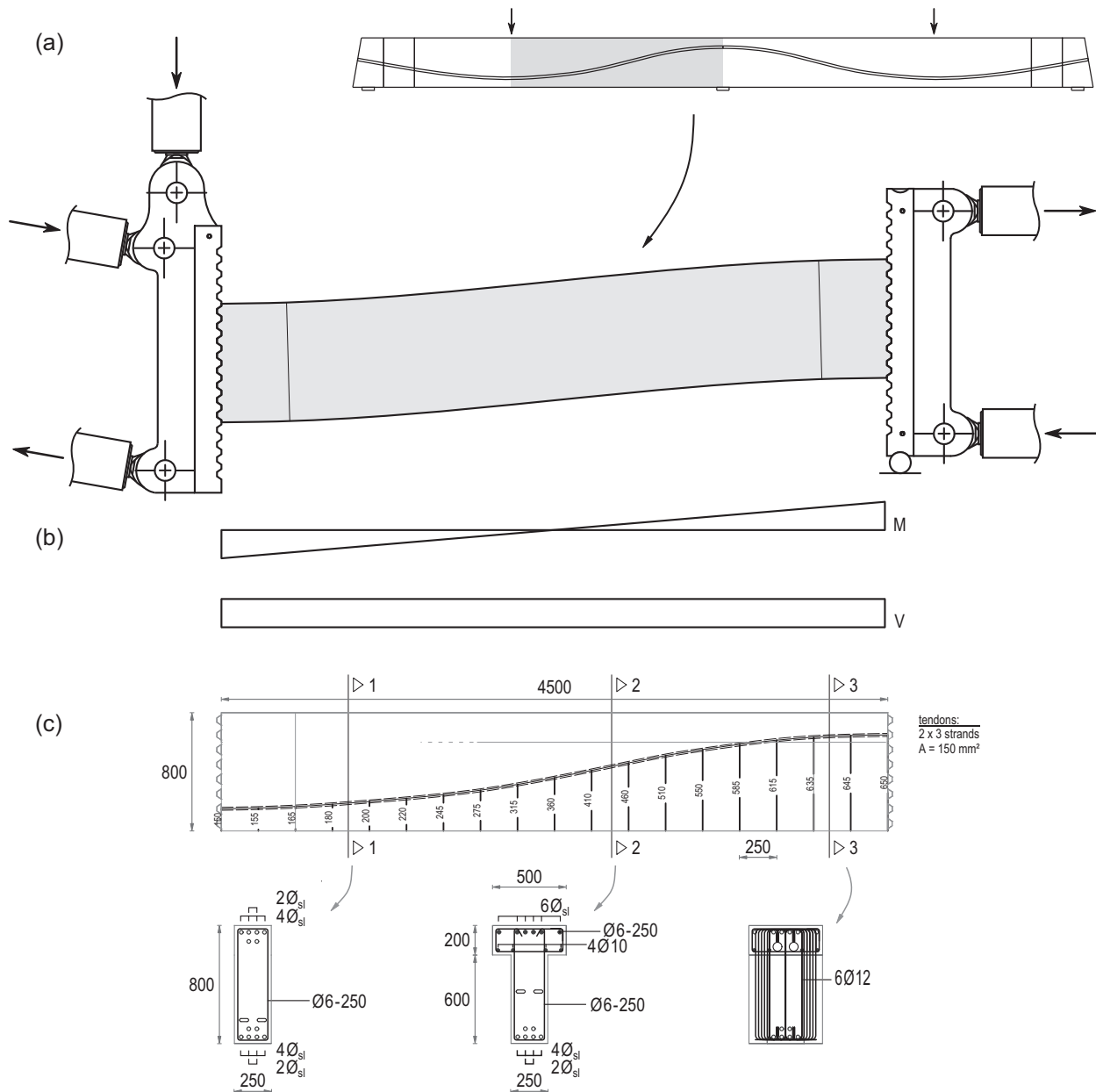


FIGURE 1 Experimental setup and focus of presented studies: (a) Substructure technique for investigating the shear strength of prestressed beam elements based on the shear field of a continuous beam between the point load in the span and the inner support. Reinforcement and tendons are anchored in tension in the cut edges/load plates. Deformed system and internal forces acting on it. The shear key profiling enables the transmission of shear forces in analogy to bridges in segmental construction. (b) Bending moment and shear force acting along the beam element. (c) Tendon layout and reinforcement detailing for investigated R- and T-shaped beam elements.

chosen diameter of the longitudinal reinforcing bars \varnothing_{sl} in the chords. In addition to the essential characteristic values of the ductile reinforcing steel bar (BSt500B), the related rib area f_{Rm} was also determined.

2.3 | Main results

All beams of the test series failed in shear. In the series of tests considered, a reduced degree of longitudinal

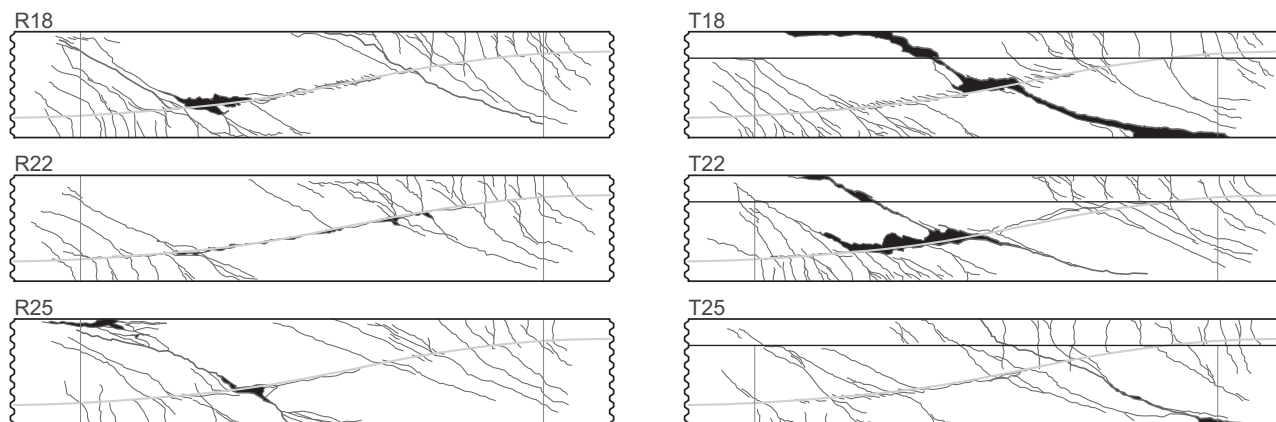
reinforcement does not adversely affect the shear capacity. This is made possible by a significant increase in strain of the initially moderately prestressed tendons. The internal force equilibrium at failure depends on general system deformation, the stiffness ratios in the tension chords and the cracked compressive stress field in the web in interaction with crossing reinforcement and tendons. The increase in strain in the tendons allows the internal equilibrium of the forces in the cut edges under maximum bending, so that even in the case of yielding

TABLE 1 Distinctive features, concrete properties and shear failure loads of the presented beam elements

ID	ρ_{sl} [–] (abs.)	$f_{c,cyl}$ (MPa)	$f_{ct,sp}$ (MPa)	E_{cm} (MPa)	σ_{cp} (MPa)	V_{max} (kN)
R25	0.016 (6 Ø 25)	41.9	3.03	28,813	2.50	483.9
R22	0.012 (6 Ø 22)	40.3	3.04	29,482	2.50	517.2
R18	0.008 (6 Ø 18)	44.4	3.04	28,631	2.50	584.6
T25	0.016 (6 Ø 25)	41.9	3.54	27,959	2.50	509.9
T22	0.012 (6 Ø 22)	53.7	3.67	31,263	2.50	609.3
T18	0.008 (6 Ø 18)	43.8	3.84	28,591	2.50	578.8

TABLE 2 Mechanical properties of used reinforcement and strands

Øs (mm)	$E_{s/p}$ (GPa)	$R_{s/p,0.2}$ (MPa)	R_m (MPa)	A_{gt} (%)	A_{10} (%)	f_{Rm} (–)	f_{Rm}/f_{Rnorm} (–)
6	200.0	531.2	601.1	5.38	14.10	0.062	1.59
18	203.0	536.5	638.5	11.53	17.33	0.079	1.41
22	198.9	522.9	633.6	12.08	19.60	0.070	1.25
25	214.3	519.8	639.9	10.88	19.20	0.056	1.05
15.7	199.5	1813.0	1946.0	5.74	6.70		


FIGURE 2 Crack patterns of test specimen at ultimate state.

reinforcing steel, the load path is ultimately defined by a shear failure. Bending cracks, shear cracking in general and the development of critical shear cracks, which ultimately limit the shear capacity with severe crack opening and stirrup rupture, in particular occurred in both field and support areas over the test series, see Figure 2. Basically, with the applied internal forces (Section 2.1), similar loading conditions exist in the field and support areas. The strains in the extreme fibers of the cross-section naturally diverge in T-beam cross-sections due to the profiled compression zone under positive bending moment. The rectangular cross-sections R25 and R22 form the final critical shear cracks in the field at load introduction. The flexural shear crack tightens the compression zone progressively as the crack root turns off strongly, which

ultimately results in a combined shear compression failure. All T-beam cross-sections, on the other hand, show a failure-initiating shear tensile crack in the support zone, which crosses the tendon and, in case of T22 and T18, does not continue at the lower edge of the flange, but even enters far into the flange. In all tests, after initial shear cracking, a further increase in load is possible, whose difference to the ultimate load is at least equal to the shear cracking load. Consequently, a reduced degree of longitudinal reinforcement significantly reduces the gap between bending and shear failure and does not lead to a completely brittle shear failure without failure indication, as a pronounced crack pattern can develop despite reduced longitudinal reinforcement and a very light shear reinforcement ratio. However, with the onset

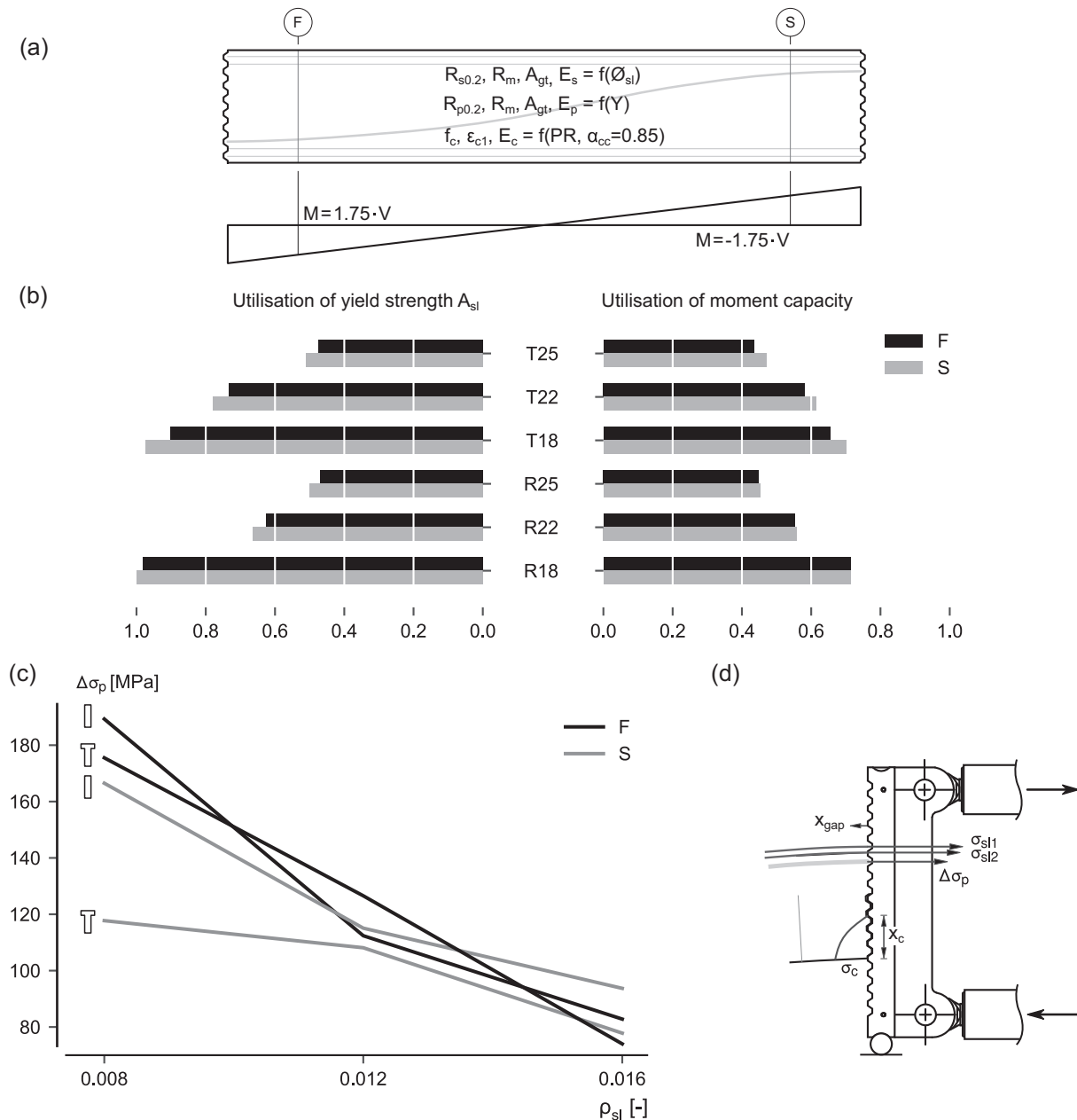


FIGURE 3 Extent of utilization in limiting sections of the shear span of constant width under bending: (a) Definition of considered sections and assumptions made in the scope of the iterative evaluation of the strain plane to determine the load-bearing capacity in considered sections F and S; (b) Utilization rates of the tension chord reinforcement A_{sl} and the complete cross-section over the test series; (c) Tendon stress increase $\Delta\sigma_p$ as a function of cross-section shape and degree of longitudinal reinforcement ρ_{sl} per cut edge; (d) Influence parameters for the evaluation of the stress increase, exemplarily shown for the cut edge of the supporting moment.

of final shear cracking kinematics, the released energy can only be damped by the stiffness of the chords and the crossing tendons, which is why the fracture of the tests with the lowest degree of longitudinal reinforcement show a particularly abrupt character.

The tests were accompanied by an extensive measurement setup. Conventionally recorded forces of the hydraulic cylinders and resulting global section forces, continuous vertical deformation and horizontal joint

opening as well as strains on the concrete surface from strain gauges are supplemented by fiber-optic quasi-continuous strain measurement along the longitudinal reinforcement and in the tendon. This information is not elaborated within the scope of this paper in order to limit the extent. In addition, tentative tests were carried out with smooth longitudinal reinforcement without ribs, which also resulted in a shear failure due to a considerable increase in the strain of the tendons. These tests are

also not discussed in this paper. Before, as already mentioned, the focus is set on the analysis of digital image data and the associated description of the crack kinematics, the internal force equilibrium at cross-section level under failure load is to be shown for the considered longitudinal reinforcement levels.

2.4 | Considerations at cross section level

For further evaluation of the shear strength characteristics, an overview of the stress ratios at the edge cross-sections of the shear span of constant cross-section width adjacent to the haunches and load plates is given. Taking into account the applied global forces and the post-tensioned tendons, the reinforcing steel in the tension chord reaches its yield strain in the support area of the tests R18 and T18, (see Figure 3b). This consideration at cross-section level is conservative as the increased strain of the reinforcement due to tension shift is not taken into account. Quasi-continuous fiber-optic measurement of the strain along the longitudinal reinforcement confirms that. Here, a shifted curve is formed corresponding to cover the envelope of tensile force due to bending. In addition to the test-specific material parameters for concrete and longitudinal reinforcement, the immediate prestress losses are taken into account. Since the prestressing is carried out starting from the cut edge of the supporting moment, a slightly lower prestressing due to wedge slip remains. Figure 3b shows the mobilization of the stepped longitudinal reinforcement level and the global cross-sectional capacity under achieved shear capacity.

Parallel to the tests on prestressed beam elements, small-scale tests were also carried out on strands grouted in ducts. The evaluation of the bond behavior and corresponding strain in the robust optical measuring fiber embedded in the grouting mortar are used in the evaluation of the different bond characteristics of the longitudinal reinforcement and the strands. In addition, the bond length is estimated in this consideration and the free length of the strands up to the anchorage in the perforated disc at the back of the counterfort is included. The tests show that even with considerably reduced longitudinal reinforcement and the yielding of the same, the bending capacity of the exposed cross-sections does not necessarily become critical if sufficient prestressing steel area is present and the corresponding increase in strain can be mobilized here. The total cross-sectional area of the prestressing steel of 900 mm² corresponds to a share of just under 2/3 of the mechanical longitudinal reinforcement degree (cf. Equation 1) at the lowest degree of

longitudinal reinforcement (R18 and T18 with $\rho_{sl} = 0.8\%$), while at $\rho_{sl} = 1.6\%$ the share is 50%.

$$\omega = \frac{\sum (A_{sl,i} \cdot R_s) + A_p \cdot R_{p,0.2}}{A_c \cdot f_{c,cyl}} \quad (1)$$

It becomes clear that the constant prestressing steel area has a high influence on the strength and the deformation capacity of the mixed-reinforced tension chord, which gains additional complexity due to the deviating, softer bond properties of the post-tensioned tendons. However, the given proportions are to be considered as theoretical upper limits, as the prestressing steel remains far from its yield strength. If the yield strength of the prestressing steel is replaced by the expected tendon stresses of a maximum of 1000 MPa as measured, the proportion is in the range of 54 to 38 percent, which still underlines the influence. The internal redistribution of the chord forces can be seen in Figure 3c. From briefly explained small-scale tests on the bond behavior of the strands and the comparison of the fiber-optic sensor system with referencing integral acting forces, together with measured joint opening (x_{gap}) and estimation of a compression zone height x_c , the stress increase of the tendons $\Delta\sigma_p$ in the field and support areas can be plotted as a function of the longitudinal reinforcement level and cross-sectional shape. The stress increases derived in an indirect way on the basis of measured data seem plausible. The basic trend of increasing prestressing steel stresses with decreasing available cross-sectional area of the longitudinal reinforcement, which is correspondingly increasingly heavily stressed, is to be expected. Due to the antisymmetric moment gradient, the behavior of the field and support cross-sections can be considered equivalent. Only the T-beam cross-section in the field diverges as the degree of longitudinal reinforcement drops. Since the internal equilibrium is bound to a minimum of the internal deformation energy and thus always results in the stiffest possible internal force flow, here the resultant compressive force in the chord primarily moves upwards and optimizes the lever arm of the internal forces without placing greater stress on the tendon. The rather strong chord deformation and tendon activation have an effect on the shear stress field along the beam elements in addition to the observation on the cross-sectional level. Remaining in the view of the strain plane, an increased mean longitudinal strain ϵ_{xm} is observed in the web. In addition, a strong deflection of the compressive stress field takes place in segments at the tendon axis. In correspondence to the tendon axis, a dominant compression arch is formed, which is branched off in its extension by advancing bending shear cracks.

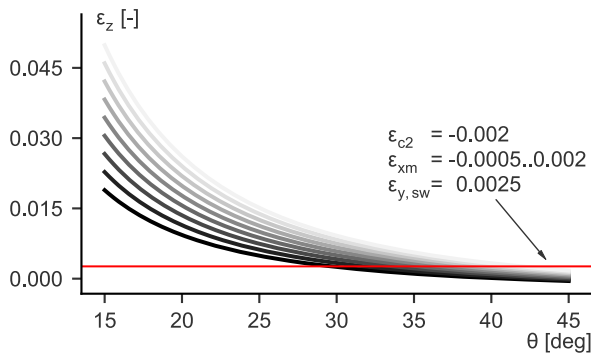


FIGURE 4 Strain in the direction of the shear reinforcement ε_z as a function of the compression field inclination θ and varying longitudinal strain ε_{xm} ; the red line marks the yield strain of the stirrup reinforcement $\varepsilon_{y,sw}$.

3 | LIMIT THOUGHTS ON THE ADEQUACY OF THE THEORY OF PLASTICITY

Approaches based on stress fields and plasticity theory provide a good basis for describing the load-bearing behavior for beam elements with sufficient shear reinforcement to ensure the assumptions of distributed fine shear cracking and sufficient ductility.^{11,23} In view of the experiments at hand an exceptional low degree of shear reinforcement did not negatively influence the necessary assumed ductility. However, the question of valid applicability of the principles and assumptions of plasticity theory and extracted truss models in particular naturally arises. In particular, a truss model with comparatively flat compression strut inclination θ does not appear compatible with the expected shear reinforcement ductility. This aspect is illustrated in Figure 4. The strain in the direction of the orthogonal shear reinforcement ε_z results on the basis of Mohr's circle of strain considering the maximum compressive strain ε_{c2} and the mean longitudinal strain of the cross-section ε_{xm} .

$$\varepsilon_z = \varepsilon_{c2} + (\varepsilon_{xm} - \varepsilon_{c2}) \cdot \cot^2 \theta \quad (2)$$

The red line corresponds to the yield strain $\varepsilon_{y,sw}$ of the bare steel. Here, tensile stiffening of the steel embedded in the concrete is not taken into account and yet it is already apparent that angles of inclination from about 27° do not appear compatible with possible strains. This is also consistent with our own experimental evidence that flat shear cracks of less than 25° , which occur before the shear strength is reached, but do not yet cause the final shear failure kinematics, can already lead to rupture of the stirrups. This means that caution is advised when applying a progressively flat compression strut angle, as such angles should possibly not be used to determine a stable load-bearing component of the shear

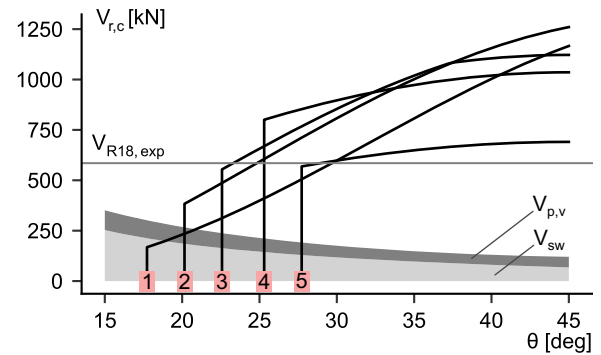


FIGURE 5 Application of selected approaches towards the reduction factor k_c on the compression field strength $V_{r,c}$ using the example of test R18. Numbering refers to Table 3; The stacked areas (shear reinforcement V_{sw} and vertical component of prestressing $V_{p,v}$, stress increase in the cut edge taken into account, cf. Figure 3d) form the lower bound solution as a function of the compression field angle θ .

TABLE 3 Different approaches to estimate the reduction factor k_c

#	Authors	k_c equation	
1	Collins ¹⁴	$1(0.8 + 170 \cdot \varepsilon_1)$	≤ 1.0
2	Muttoni ²⁴	$1(1.05 + 80 \cdot \varepsilon_1)$	≤ 0.8
3	Sigrist ^{23,25}	$1(1.2 + 55 \cdot \varepsilon_1)$	≤ 0.65
4	SIA 262; el. chords	0.6	
5	SIA 262; pl. chords	0.4	

reinforcement. The flat crack angles only occur when the crack root is strongly deviating and the compression zone is squeezed or when abrupt shear cracks occur (especially in T-beam cross-sections) close to the ultimate loads reached. The released resisting component of structure can be immediately internally redistributed with a slight drop in load in the meantime. The set of curves additionally varies the influence of the mean longitudinal strain ε_{xm} on the theoretical strain in the stirrup direction ε_z . Here it can be seen that a comparatively reduced prestress or progressive strain increase in the chords with reduced longitudinal reinforcement has an equally detrimental effect on ε_z , if the strain compatibility is to be maintained.

Figure 5 shows the listed approaches from Table 3 for reducing the concrete compressive strength in the cracked web as a function of crossing principal tensile strain ε_1 .

$$\varepsilon_1 = \varepsilon_{xm} + (\varepsilon_{xm} - \varepsilon_{c2}) \cdot \cot^2 \theta \quad (3)$$

The mean longitudinal strain ε_{xm} is calculated from the strains of the extreme fibers of the cross-section after

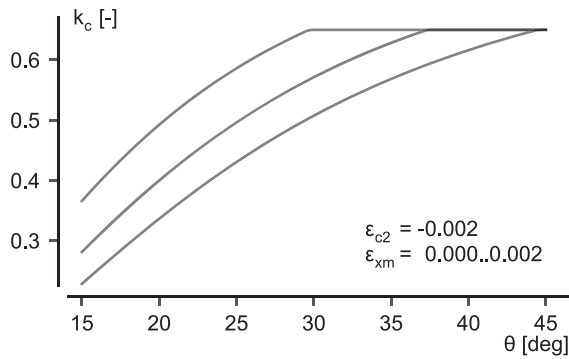


FIGURE 6 k_c as a function of the compression field angle θ evaluated for Sigrist's approach and varying strain ε_{xm} .

iterative computation of the strain plane under acting moment and normal force from prestressing and outer loading at ultimate limit state. The load-bearing components of the shear reinforcement and prestressed tendons are plotted as stacked areas depending on the compression strut inclination angle θ . The shear capacity achieved in the R18 test is also marked as an example. The order of the curves along the axis of the compression strut angle to be applied can be shifted as required. Depending on the chosen approach for k_c from Table 3, the curves represent the shear capacity of the inclined concrete compressive stress field $V_{r,c}$, the upper limit value of a possible plastic capacity.

$$V_{r,c} = b_{w,nom} \cdot z \cdot k_c \cdot \eta_{fc} \cdot f_c \cdot \sin\theta \cdot \cos\theta \quad (4)$$

Approaches 3 and 5 suggest in this case for the beam element R18, that depending on θ even a compression strut failure could be achieved, if the missing resistance delta after shear reinforcement and vertical tendon component could be explained from the plasticity theory. At this point it becomes obvious that with a low degree of shear reinforcement, the shear strength capacity of prestressed beam elements cannot be adequately described by the plasticity theory. A concrete load-bearing component, postulated in manifold ways, plays a significant role here and allows for a much more favorable system load-bearing behavior. From this perspective, the question also arises as to what relevance must be attributed to a limit on the compression strut load-bearing capacity of the cracked web panel, if the load-bearing behavior is characterized by a compression arch or by shear stresses in the bending compression zone. This aspect will be part of further considerations, but will not be pursued further in this paper.

Figure 6 shows the development of the reduction factor k_c under commonly assumed maximum utilization

of the compression strut with variation of the mean longitudinal strain, using Sigrist's approach²⁵ as an example. As can be seen from Table 3, the principal tensile strain serves as input parameter, whereby strictly speaking only an iterative solution is possible due to mutual dependence of k_c , θ and ε_1 . This circumstance is bypassed using a constant choice of the inclination angle θ and neglects the iterative problem. Equations 1–3 from Table 3 are topological similar, but differ primarily, because they were derived on the basis of different test series (panel tests/^{14,26} beam tests).²³ This is also the reason for the different maximum cutoff. The assumption $\varepsilon_{c2} = -2.0\%$ originates from the idea of the lower static load limit, according to which, in the ideal plasticity-theoretical case, concrete and shear reinforcement in the web simultaneously reach their maximum use. By means of deformation measurements in the web level, Rupf²⁷ was able to show, that the compression strain at failure essentially does not fall below $\varepsilon_{c2} = -1.0\%$. Only in the area of the tendon axis was $\varepsilon_{c2} = -2.0\%$ recorded for the comparatively thin webs. Similarly, in the experiments discussed within this contribution, on the basis of digital image correlation and discrete DMS rosettes unaffected by cracks a compression of the order of magnitude $\varepsilon_{c2} = -2.0\%$ cannot be reconstructed outside the load introduction in the haunches. This assumption is therefore another factor of uncertainty in the transfer of plasticity-theoretical truss ideas to beam elements with a low degree of shear reinforcement. The model conception does not seem to be suitable for describing the load-bearing behavior without ignoring recognizable mechanical correlations and experimental evidence.

A possible approach in the extension of the stress field analogy based on plasticity theory can be constructed by combined fans of the compressive stress field.^{28,29} Here, the originally simplified constant inclination of the compressive stress field is deviated by the tendon geometry. In addition, a slope can be attributed to the compression chord. Alternatively, and much more commonly implicit in international design standards, is the interference of a truss model and a crack friction component, making the principal strains and principal stresses nonaffine ($\theta_e \neq \theta_o$).

This idea violates a basic assumption of plasticity theory,³⁰ but is popular because of its simple and pragmatic implementation. Against its mechanical background, this idea is strongly coupled to the shear cracking behavior of the web and thus has to be considered in ambivalence for high and low shear reinforcement levels. The derivation of crack-bridging forces requires a minimum crack opening and predominantly tangential displacements along the crack path. This idea

underlies at least the small-scale tests that contributed to the derivation of the aggregate interlock relationships.³¹ The characteristic cracking behavior of the prestressed beams and a verification of these assumptions in the presence of a low shear reinforcement ratio are presented in the next section.

4 | CONSIDERATIONS ON CRACK KINEMATICS

4.1 | Digital image correlation setup

The test series was accompanied by an exhaustive measurement programme. In the following, key results based on digital image correlation are illustrated. Digital image correlation was used to record concrete deformation and cracking processes across the full span of the beam element of constant web width. For this purpose, the web surface was given a stochastic pattern across the span. The evaluation based on the relative displacements of the pixel facets and subset deformations allows a continuous view of the spatially varying principal deformations on the surface of interest, which can be attributed a plane state of stress. Local effects originating from a deviation of the compression field along the tendon axis are excluded at this point. In the course of the tests, two 2D systems were used to ensure a sufficient resolution of about 2 pixels per millimeter over the complete width of approx. 3.5 m of the area to be covered. Images were taken every 5 s. After performing a perspective transformation of the image data, which unifies the normal vector of the observed surface with the lens' viewing axis, the digital image correlation was performed. The DIC formulation used has a robust kernel cross-correlation and uses nonlocal gradients, so that even in the case of strong discontinuity development due to crack formation, the distortions can be calculated consistently.¹⁵ The quality of the correlation and the reliability of the absolute weight calculation depends largely on the choice of the parameters gauge size, subset size and step size, which is always a trade-off between reduced noise and the detection of sharp peaks of deformation (accuracy). Based on the pixel displacements and grouping them into subsets, Green-Langrange distortions E_{xx} , E_{yy} and associated shearing E_{xy} can be determined. The transformation of the results into distortions subsequently allows the calculation of the principal strain ϵ_1 , which is used in further analysis as an indicator of discrete crack width. Recalling Mohr's circle of strain, these relationships are expressed in the following terms.

$$\begin{aligned}
 \epsilon_x &= E_{xx} \\
 \epsilon_y &= E_{yy} \\
 \gamma_{xy} &= E_{xy} \cdot 2 \\
 \epsilon_1 &= \frac{1}{2} \cdot (\epsilon_x + \epsilon_y) + \frac{1}{2} \cdot \sqrt{(\epsilon_y - \epsilon_x)^2 + \gamma_{xy}^2}
 \end{aligned} \tag{5}$$

Since a virtual strain gauge (VSG) is based on a polynomial fit along pixel subsets the larger the environment, the more pronounced the smoothing of deformation values. Conversely this also means that peaks and thus details of the measurement data are increasingly reduced.¹⁶ In the context of these investigations, a good compromise could be achieved with the settings in Table 4 with regard to the above-mentioned constraints.

For influencing factors and possible blurring in the course of the application and evaluation of digital image data, refer to ref. 32.

4.2 | Crack kinematics processing

In the following, the essential steps in the processing of the image data for the evaluation of the crack kinematics are explained. A chronological overview of the elements can be found in Figure 7. Image normalization is used to increase the contrast of a DIC step to enable better extraction of crack contour features of an image. This step also removes noise from the image. While this procedure falsifies the absolute measured relative pixel displacements, it's important to state, that this step is not the base for a further evaluation of the principal strains, but only serves as a basis for the recording of the geometric crack contours. Thresholds on the pixel array are based on the median ν of the single channel pixel intensities. Lower and upper bounds are formulated as:

$$\begin{aligned}
 low &= \max \{ (1.0 - \sigma) \cdot \nu, 0 \} \\
 high &= \min \{ (1.0 + \sigma) \cdot \nu, 255 \}
 \end{aligned} \tag{6}$$

The standard deviation is assumed to be $\sigma = 0.33$, which has proven to be a robust value for isolating the crack contours. In case of unfavorable exposure or noise within the image data, this value may have to be adapted. Using morphological methods of image processing,^{33,34} the center line of the extracted crack contour surfaces can be determined, which naturally can also branch out as usually observed in concrete. Since the automatically generated crack network is defined on the basis of polygonal grid points with irregular spacing, the crack path is regularized for further evaluation, so that the subsequent evaluations show a homogeneous data density.

TABLE 4 Essential parameters in the process of digital image correlation; further details on the implementation are found here.^{15,16}

Parameters	Settings
Gauge size	30 px
Subset size	23 px
Step size	10 px
Shape function	Affine
Interpolation routine	Cubic convolution
SSSIG threshold	50

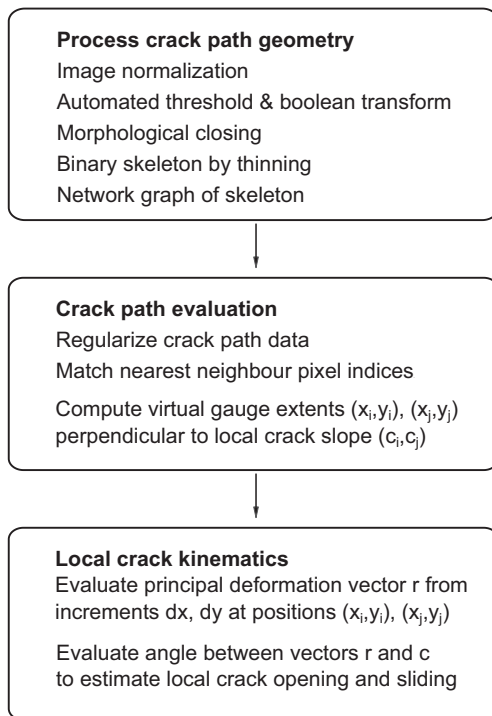


FIGURE 7 processing steps on crack kinematics.

A homogeneous path t from arbitrarily spaced raw contour points can be constructed by cumulative summing of all discrete differences and subsequent independent interpolation of the x - and y -coordinates with respect to the new coordinates.

$$t_k = \sum_{i=1}^k \|(\Delta x, \Delta y)\| \quad (7)$$

The equally spaced crack contour provides the indexing filter for extracting translations u, v (refer to Figure 8) and principal strain ϵ_1 from true DIC data. The main distortions are evaluated along a VSG perpendicular to the crack path. The length of the VSG is chosen to 30 pixels, so that the information is acquired outside the discontinuous crack contour and is less likely to be affected by

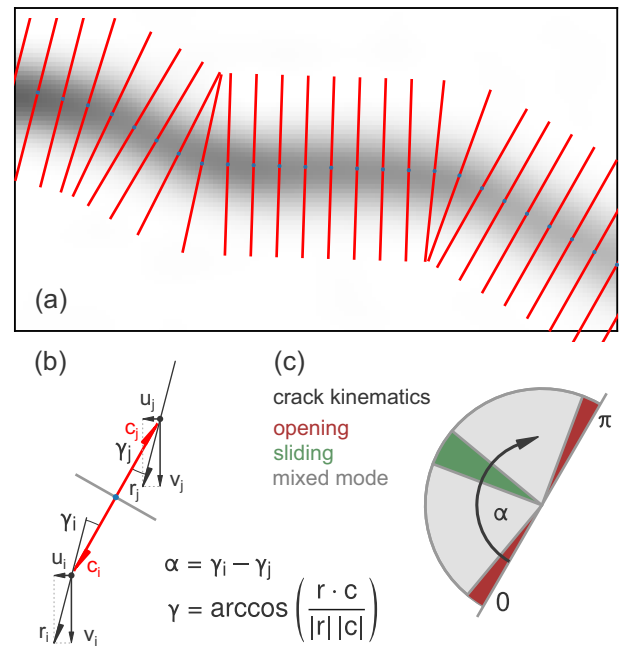


FIGURE 8 Evaluation of local crack kinematics a) Regularized crack contour and orthogonal distance units for tapping the relative displacements u and v ; b) Definition of the vectors and angular references under discussion; c) Illustration of the difference angle α from crack edge movement and resulting impact on the transfer of stresses across cracks. The intervals exclusive of the mixed mode each take up a total of 20° and have only a pictorial meaning here.

local minima of the correlation quality in the high strain area of opening cracks.¹⁵

The character of the crack kinematics can now be assessed on the basis of the vectors \mathbf{c} and \mathbf{r} , whereby the difference of angle results from the isolated comparison per crack edge. If the direction of the crack normal corresponds to the translation vector \mathbf{r} , dominant crack opening on at least one side without any components from sliding takes place. The synthesis of this approach can be converted into a statement on the dominant fracture mode. The following section employs the outlined strategy of data preprocessing and evaluation and illustrates for selected test specimens with different cross-sections and varying longitudinal reinforcement essential key points in the context of the contentiously discussed description of possible load-bearing components from aggregate interlock as a component of the global shear capacity of a beam system.

4.3 | Investigations in the context of potential shear transfer mechanisms arising from aggregate interlock

The crack kinematics and the character of the fracture processes are discussed within the context of the present paper for the largest and lowest longitudinal

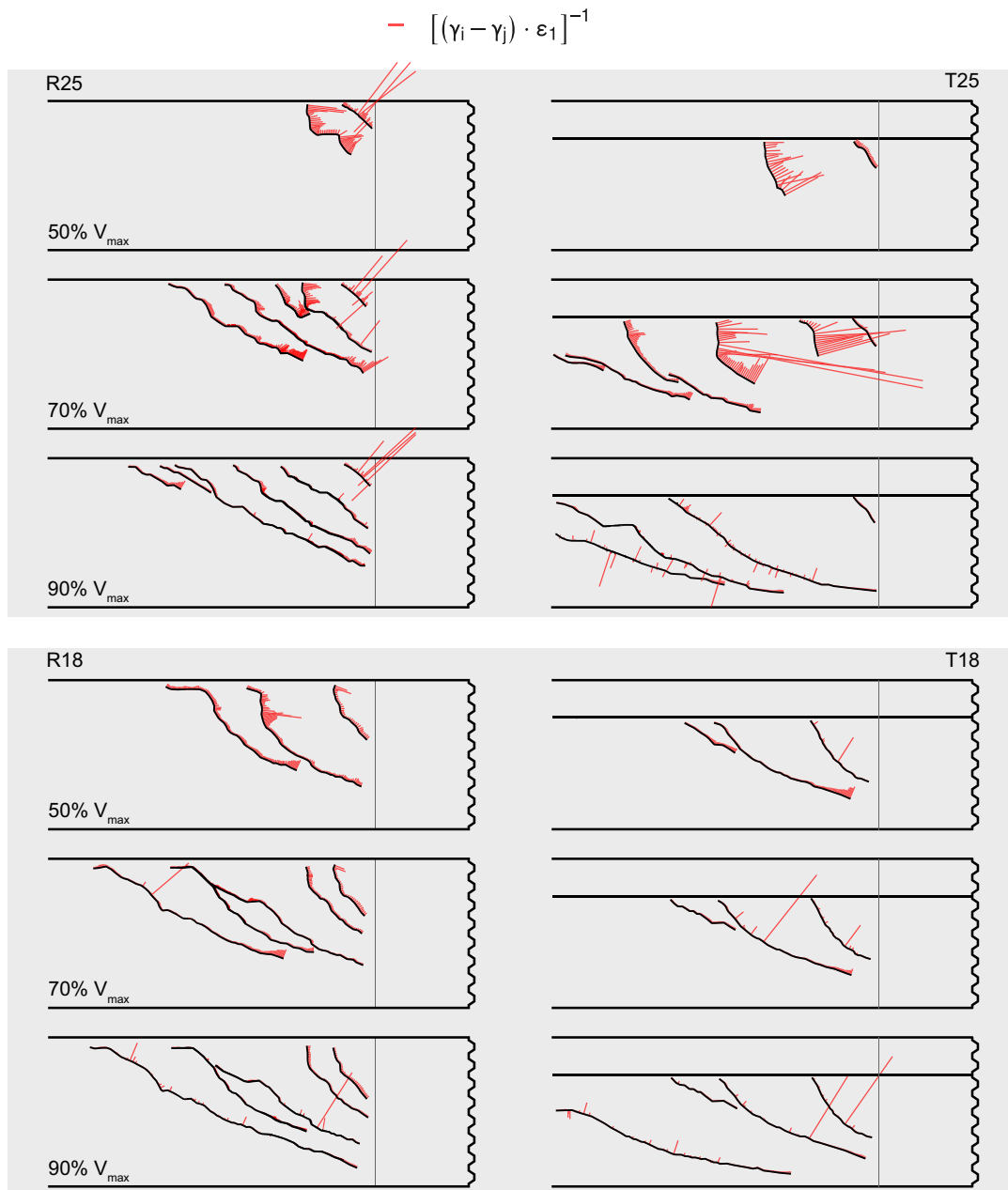


FIGURE 9 R25, R18 and T25, T18 fracture mode analysis based on local crack angles in correspondence to evaluated deformations along crack edges and principal strains from digital image correlation.

reinforcement ratio for rectangular and T beam cross-sections. Figure 9 shows the reciprocal of the difference angles along significant crack paths for a load level, scaled by the principal strains ε_1 from DIC data. The length of the red lines thus increases to the reciprocal of the local crack width and thereby indicates crack segments whose crack opening is sufficiently small to be able to transmit forces - if there is a dominant sliding crack edge displacement at all. The cracks shown over the load levels vary slightly in some cases because only the main cracks under the respective load level are evaluated with an automated threshold, cf. section 4.2. This

procedure reduces the crack pattern to the essential crack contours and does not falsify the impression, as a possibly slight crack and its increased proportion of recorded crack sliding cannot contribute to a global load-bearing fraction related to aggregate interlock, if it is adjacent to massive shear crack opening in the web. The beam elements R25 and T25 with a high degree of longitudinal reinforcement may still be able to serve load-bearing components from the phenomenological viewpoint of crack interlocking under moderate load levels; in the case of the T-beam cross-section, this seems even more feasible. Under increasing load and upon reaching the

ultimate limit state, the crack edges move apart almost exclusively in accordance with the concept of fracture mode I. Rare peaks, artifacts of the fine discretization along the crack path, have no mechanical significance. A true order of magnitude of interlocked cracks to describe the effective load-bearing mechanisms at the ultimate load level does not seem justified. That is made all the more evident for R18 and T18, which have a comparatively low degree of longitudinal reinforcement and appear representative for economically designed bridge cross-sections. Here, reduced crack branches that do not open with priority form only in a limited number of cases, mostly in accordance with the decreasing gradient along the crack process zone starting from the crack root.³⁵ Different fracture mechanics approaches can also be applied in this domain. In particular, recent investigations involving compressive stresses parallel to the crack contour offer a possible approach here.³⁶ Therefore the application of widely used aggregate interlock model concepts^{31,37} to determine an associated resulting global load-bearing component is, in the opinion of the authors, not appropriate. Formulating partial components of structural capacity on this basis bypasses the control of system equilibrium. In doubt, this overestimates the contribution from aggregate interlock and implicitly leads to a wrong way of thinking in the assumption of a model conception of a derived internal load-bearing response. Further considerations and discussions on the limits of the physical background for a model approach grasping the aggregate interlock phenomena can also be found in other recent studies.³⁸⁻⁴⁰ These hypotheses are based on one hand on the phenomenological assumptions of aforementioned investigations on small-scaled tests and on the other hand on the evaluations of presented tests using digital image correlation and the evaluation of discrete crack kinematics.

The definition of possible crack-bridging forces on the basis of the local variation of crack sliding and crack opening provides an elegant basis for linking different boundary conditions in a generalized model, augmented by empirical factors. However, the test arrangements used (push-off tests, direct shear tests) are suitable to a limited extent, since prefractured crack lips and a path-independent development of the crack kinematics (see ref. 41) cannot do justice to the cracking processes of a full scale beam structure. Walraven³¹ assumes that crack opening and sliding form consecutive processes, which does not coincide with general and also the author's own experimental observations. In particular, the assumption of predominant crack sliding of the separated edges after initial crack formation (and thus justifies the load-bearing component from crack friction) cannot be confirmed on the basis of the evaluation of the experimental

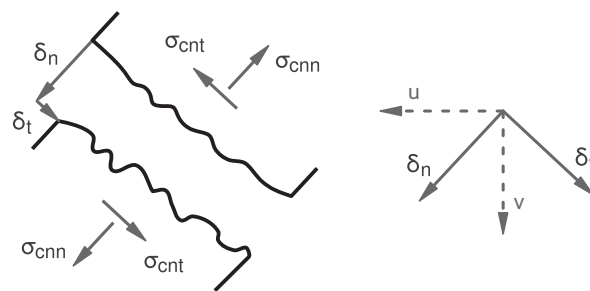


FIGURE 10 Common convention of relative displacements at the crack and derived stress components; the relative displacements are formulated at a locally variable coordinate system along the crack.

data. The results are of course primarily limited to the parameters of the test schedule. With a different maximum aggregate size, a high degree of shear reinforcement and the associated limitation of the shear crack widths, the impact of crack interlocking can be more significant. With such a weak shear reinforcement ratio and large longitudinal strains, aggregate interlocking is to a certain extent self-excluding in the ultimate limit state. Even independent of shear reinforcement keeping the crack widths minimal, the surface roughness and thus the maximum aggregate size can have a considerable influence on the shear force transfer, especially in comparatively steep crack sections.⁴² In the focus of tests carried out against the background of prestressed bridges in existing structures with exceptionally low-shear reinforcement ratios, however, the results complement and confirm previous investigations^{2,6,43} on prestressed concrete beams, which reveal a strongly decreasing proportion of possible load-bearing components from crack friction under increasing load. The basic assumption, that the parameters describing the load-bearing mechanisms across cracks in concrete - namely δ_n , δ_t , σ_{cnt} and σ_{cnn} as briefly illustrated in Figure 10 - are assumed to be smeared over a larger cracked domain, is mainly due to the limitations of the experimental tests used to derive these relations.

Figure 11 shows the macroscopic evolution of the dilatancy a_d along the critical crack contours at selected load levels, as shown in Figure 9. The dilatancy ratio a_d of local crack opening and crack sliding shows characteristic deviations for the investigated longitudinal reinforcement ratios for the considered tests and selected load levels. With a heavy degree of longitudinal reinforcement (R25 and T25), many critical crack paths show a dominant crack opening ($a_d \geq 1$). At about 90% of the ultimate load, the median of the dilatancy ratio of all cracks considered falls below 1, and thus the character of the crack kinematics is stronger defined by a local

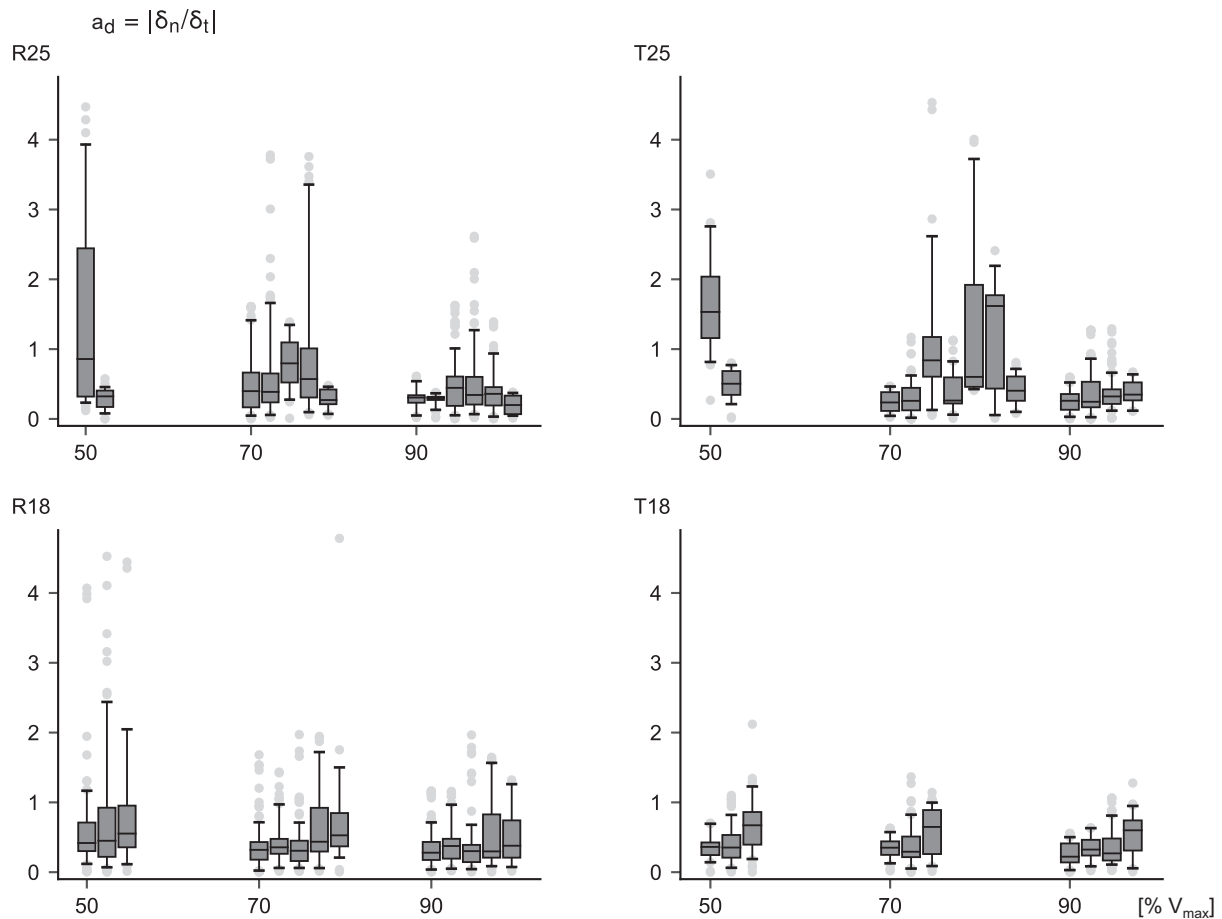


FIGURE 11 crack dilatancy as a function of crack kinematics.

parallel displacement of the crack sides or a global rotation around the crack tip. At this stage, however, the crack widths are already in the order of 2 to 3 mm. Therefore effective crack interlocking can no longer play a role despite decreasing dilatancy. With reduced longitudinal reinforcement ratio (R18 and T18), the interquartile range shows a significantly lower variance within the discrete dilatancy ratios along the crack paths. Here, a more pronounced crack opening already takes place at a lower load level, since the reduced longitudinal reinforcement in the tension chord experiences high strains at an earlier stage.

Irrespective of the degree of longitudinal reinforcement and the shape of the cross-section, it can be stated that the assumption of strictly consecutive movement of the crack sides, as assumed by Walraven³¹ for example and applied in abstracted push-off tests, cannot be reproduced on the basis of the data from the digital image correlation of full-scale beam tests, which allow for a phenomenologically properly scaled development of the crack formation processes. An example of this may be the web of the support area of the test beam T18 immediately before and after abrupt failure of the

already distinctive and wide-open critical shear crack, see Figure 12.

Under large deformation and plastic strain of the longitudinal reinforcement in the chord, the beam forms progressively flatter shear cracks proceeding into the support area, which initially develop as bending shear cracks. When the ultimate limit state is in sight, the compression arch tries to flatten more and more, which leads to final critical shear tension cracks in the web, which finally progress into the compression zone below to such an extent that the internal equilibrium can no longer be maintained and kinetic energy is abruptly released.

5 | MODEL COMPARISON

Finally, the ultimate loads of presented tests are briefly compared to the estimations of two shear strength models. Figure 13 shows the normalized shear capacity of the beam elements, classified by cross-sectional shape and degree of longitudinal reinforcement. In comparison, the load-bearing capacity was determined according to the Flexural Shear Crack (FSC) Model^{2,44} and the

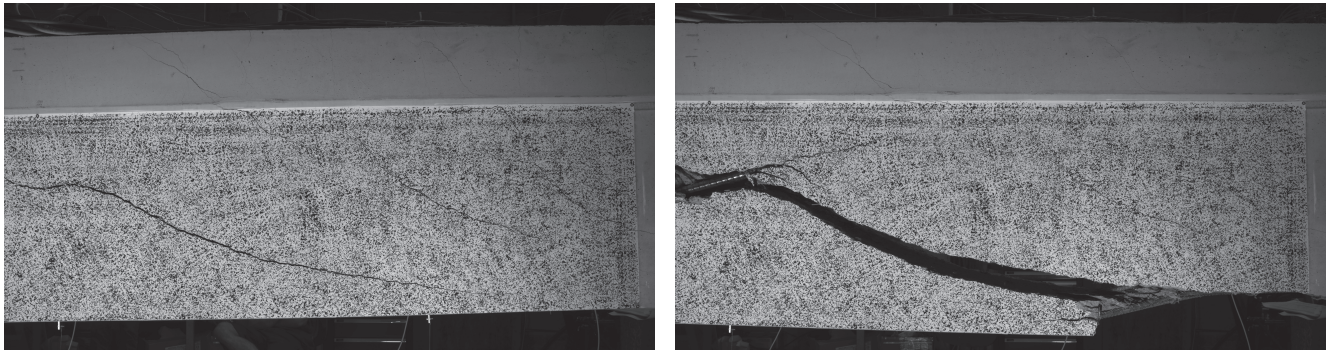


FIGURE 12 T18 in the support moment area imminent before sudden failure and final crack pattern.

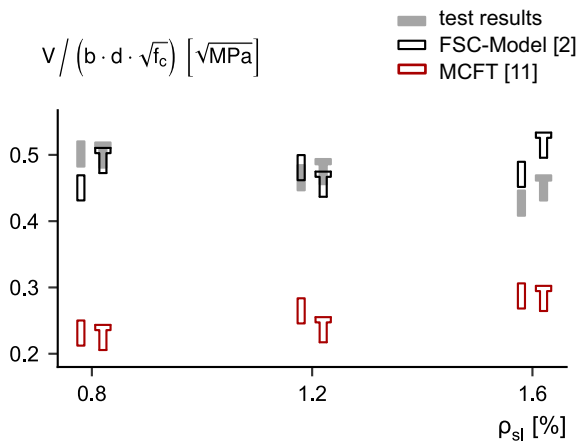


FIGURE 13 Normed shear capacity of tested beam elements compared to selected shear strength models.

Modified Compression Field Theory (MCFT).¹⁴ While the latter bases the concrete load-bearing component on aggregate interlock, supplemented by empirical model factors, the FSC model allows considering of a load-bearing component of the concrete compression zone, which is limited by a biaxial failure criterion, if the degree of prestressing is sufficient. In the general procedure of the FSC model, the analysis section is determined by iterative computation. For the MCFT analysis, internal forces, distortions and tendon inclination were considered at a distance d from the beginning of the haunch in the support area. A significantly better assessment quality is shown under the assumption that shear stresses in the concrete compression zone can describe the shear strength of prestressed beams with a low degree of shear reinforcement complementing the comparatively low truss mechanisms of the stirrup reinforcement and the vertical component of the tendons.

It should be explicitly stated once again that a prediction is not suitable as a measure of an explanation or plausibility check, since one can draw perfectly precise predictions from an incorrect model. Only mechanically

consistent models that build on causal relationships appear trustworthy, since the sample size of experimental evidence can never be sufficient, even with explicit model restriction. As already demonstrated from various perspectives on all possible questions, that boil down to a description of the shear strength and mechanisms in structural concrete,^{38,41,45} the description of the load-bearing behavior on the basis of the compatibility of the overall strains appears to be the most logical approach. Of course, a trade-off must be struck between the necessary complexity and practical aspects.

6 | CONCLUSIONS

Within the scope of the presented investigations, structural tests were carried out on prestressed beam elements under variation of the longitudinal reinforcement ratio. Even in the case of plastic strain occurring in the longitudinal reinforcement due to bending, the system load-bearing capacity was always limited by a shear failure. The ultimate failure can essentially be classified as a bending shear failure, taking into account the entire loading history. Under strong crack opening, the stirrups rupture. In particular, the T-beams show increased tensile shear cracking in the already cracked compressive stress fields in the span and support areas before the failure load is reached. At ultimate limit state the final fracture is localized in a critical bending shear crack or in an intrusive shear crack. The energy released can only be damped by the stiffness of the chords or the crossing tendon, which is why the fracture of the tests with the lowest degree of longitudinal reinforcement shows a particularly abrupt character. In the course of the analysis of the test results, starting from the prevalent strain state at cross-section level and in the compressive stress field of the cracked web, considerations are first made about possible framing in the perspective of plasticity theory, see section 2.4 and 3. Furthermore, digital image

correlation data was used for an in-depth analysis of the development of crack kinematics and evaluated in the context of common models for the description of a possible load-bearing component derived from aggregate interlock. On the basis of the tests, the data interpretation presented and the model comparisons carried out, the following can be stated:

- A reduced degree of longitudinal reinforcement does not adversely affect the shear capacity. This is enabled by a significant increase in strain of the initially moderately prestressed tendons, cf. Section 2.2. The internal force equilibrium under failure depends on principal strains within the beam system, the stiffness conditions in the tension chords and the cracked compressive stress field in the web in interaction with crossing reinforcement and tendons. The increase in strain in the tendons allows for the static equilibrium in the cut edges under maximum bending, so that even in the case of yielding longitudinal reinforcement, the load path is finally defined by a shear failure.
- Beams with low ratio of shear reinforcement only fulfill assumptions for a plasticity-theoretical perspective to a limited extent. Rotating crack models are not absolutely suitable. However, aggregate interlock components are widely used in shear model formulations, especially for members without shear reinforcement. This procedure cannot be adopted for the present experimental investigations analogous to previous, realistically scaled and adjusted test series.^{2,43,46}
- Except for the crack process zone and the immediate crack tip, no load-bearing component from aggregate interlock can be justified on the basis of DIC analysis for the considered constellation of prestressed beam elements with a low-shear reinforcement ratio. An evaluation of the crack friction with empirical models was not carried out, because such models cannot mimic the boundary conditions of a crack formation process in the structural member in an adequate way. The shortcomings lie mainly in the prefractured crack surface of the push-off bodies and the inflexible kinematics (no classical rotation around the crack tip possible).
- The model idea of a truss model and additive crack friction does not appear reasonable in case of having such a low-shear reinforcement ratio. A concrete load-bearing component should at best be described deriving the general strain state, but at least on the basis of the load-bearing capacity of the concrete compression zone due to bending.
- The comparison of the experimental ultimate loads with selected model approaches having different philosophies in weighting dominant influencing factors

(see Chapter 5) shows that an explicit concrete bearing component can be mechanically justified and forms a promising approach in the context of evaluating prestressed concrete bridges with a low-shear reinforcement ratio.

ACKNOWLEDGMENTS

The authors thank the Federal Highway Research Institute of Germany for their financial support of this research.

CONFLICT OF INTEREST STATEMENT

The authors declare no potential conflict of interests.

DATA AVAILABILITY STATEMENT

The data that support the findings of this study are available from the corresponding author upon reasonable request.

ORCID

Sebastian Thoma  <https://orcid.org/0000-0001-8829-512X>

REFERENCES

1. Schramm N, Fischer O. Zur Anrechenbarkeit von nicht norm-gemaßen Bilgelformen auf die Querkrafttragfähigkeit von Bestandsbrücken. *Bauingenieur*. 2020;95(11):408–18.
2. Huber P, Huber T, Kollegger J. Experimental and theoretical study on the shear behavior of single- and multi-span T- and I-shaped post-tensioned beams. *Struct Concr*. 2020;21(1):393–408.
3. Adam V, Herbrand M, Hegger J. Querkrafttragfähigkeit von Brückentragern aus Spannbeton mit geringen Querkraftbewehrungsgraden. *Bauingenieur*. 2020;95(11):397–407.
4. Gleich P, Kattenstedt S, Maurer R. Erweitertes Druckbogenmodell für die Bestimmung der Querkrafttragfähigkeit von Stahl- und Spannbetonbalken. In: *Beton- und Stahlbetonbau*. 2016; 111(5):268–77.
5. Gleich P, Maurer R. Das Erweiterte Druckbogenmodell für die Nachrechnung von Spannbetonbrücken - Theoretische Hintergründe. *Bauingenieur*. 2020;95(11):430–9.
6. Herbrand M. "Shear strength models for reinforced and prestressed concrete members." PhD thesis. RWTH Aachen. 2017.
7. Tompos E, Frosch RJ. Influence of beam size, longitudinal reinforcement, and stirrup effectiveness on concrete shear strength. *ACI Struct J*. 2002;99:559–67.
8. Lubell AS, Bentz EC, Collins MP. Influence of longitudinal reinforcement on one-way shear in slabs and wide beams. *J Struct Eng*. 2009;135(1):78–87.
9. Khaja MN, Sherwood EG. Does the shear strength of reinforced concrete beams and slabs depend upon the flexural reinforcement ratio or the reinforcement strain? *Can J Civ Eng*. 2013;40(11):1068–81.
10. Monserrat Lopez A, Fernandez Ruiz M, Miguel Sosa PF. The influence of transverse reinforcement and yielding of flexural reinforcement on the shear-transfer actions of RC members. *Eng Struct*. 2021;234.

11. Muttoni A, Schwartz J, Thiirlimann B. Design of Concrete Structures with Stress Fields. Basel, Switzerland: Birkhauser; 1997.
12. Yang Y. "Shear behaviour of reinforced concrete members without shear reinforcement: A new look at an old problem." PhD thesis. TU Delft. 2014.
13. Mari A et al. Shear-flexural strength mechanical model for the design and assessment of reinforced concrete beams subjected to point or distributed loads. *Front Struct Civ Eng*. 2014;8(4):337–53.
14. Collins MP et al. A general shear design method. *Struct J*. 1996; 93(1):3645.
15. Lehoucq RB, Reu PL, Turner DZ. A Novel Class of Strain Measures for Digital Image Correlation. *Strain*. 2015;51(4):265–75.
16. Turner DZ. An overview of the virtual strain gauge formulation in DICe. Tech rep. 2018.
17. Schramm N, Fischer O. Querkraftversuche an profilierten Spannbetontragern aus UHPFRC. *Beton-und Stahlbetonbau*. 2019;114(9):641–52.
18. Kaufmann W, Marti P. Versuche an Stahlbetontragern unter Normal- und Querkraft. Basel, Switzerland: ETH Zurich; 1996.
19. Kani GNJ. The riddle of shear failure and its solution. *J Am Concr Ins*. 1964;61(4):441–68.
20. Schramm NO. "Zur Querkrafttragfähigkeit von Spannbetonbalkenelementen unter besonderer Berücksichtigung der BÜgelform." PhD thesis. Technische Universität München. 2021.
21. CEN. Eurocode 2: Design of concrete structures - Part 2: Concrete bridges - Design and detailing rules European Committee for Standardization. 2010.
22. Herbrand M, Classen M, Adam V. Querkraftversuche an Spannbetondurchlauftragern mit Rechteck- und I-Querschnitt. *Bauingenieur*. 2017;92:465–73.
23. Kaufmann W. "Strength and deformations of structural concrete subjected to in-plane shear and normal forces." PhD thesis. ETH ZÜRICH. 1998.
24. Fernandez Ruiz M, Hars E, Muttoni A. Resistance a l' effort tranchant des poutres precontraintes a times minces. Bern, Switzerland: EPFL; 2006.
25. Sigrist V. Generalized stress field approach for analysis of beams in shear. *Struct J*. 2011;108(4):479–87.
26. Belarbi A, Hsu TTC. constitutive laws of softened concrete in biaxial tension compression. *Struct J*. 1995;92(5):562–73.
27. Rupf M. "Querkraftwiderstand von Stahlbeton- und Spannbetontragern mittels Spannungsfeldern." PhD thesis. EPFL. 2014.
28. Stoffel P. "Zur Beurteilung der Tragsicherheit bestehender Stahlbetonbauten." PhD thesis. ETH ZÜRICH. 2000.
29. Zwicky D. "Zur Tragfähigkeit stark vorgespannter Betonbalken." PhD thesis. ETH ZÜRICH. 2002.
30. Muttoni A. Die Anwendbarkeit der Plastizitätstheorie in der Bemessung von Stahlbeton. Vol 176. Basel, Switzerland: Birkhauser; 1990.
31. Walraven J. Aggregate Interlock: A theoretical and experimental analysis. Delft University Press; 1980.
32. Mata-Falcon J et al. Combined application of distributed fibre optical and digital image correlation measurements to structural concrete experiments. *Eng Struct*. 2020;225:1–17.
33. van der Walt S et al. scikit-image: image processing in Python. *PeerJ*. 2014;2.
34. Bradski G. "The OpenCV Library." *Dr. Dobb's Journal of Software Tools*. 2000.
35. Zink M. Zum Biegeschubversagen schlanker Bauteile aus Hochleistungsbeton mit und ohne Vorspannung. Wiesbaden, Germany: Vieweg+Teubner Verlag; 2000.
36. Hoang N et al. New perspective of fracture mechanics inspired by gap test with crack-parallel compression. *Proc Nat Acad Sci*. 2020;117(25):14015–20.
37. Gambarova PG, Karakoc C. A new approach to the analysis of the confinement role in regularly cracked concrete elements. *IASMiRT*. 1983;251–61.
38. Beck A. "Paradigms of shear in structural concrete: Theoretical and experimental investigation." PhD thesis. ETH Zürich. 2021.
39. Pundir M et al. Review of fundamental assumptions of the two-phase model for aggregate interlocking in cracked concrete using numerical methods and experimental evidence. *Cement Concr Res*. 2019;125.
40. Volgyi I, Windisch A. Experimental investigation of the role of aggregate interlock in the shear resistance of reinforced concrete beams. *Struct Concr*. 2017;18(5):792–800.
41. Cavagnis F. "Shear in reinforced concrete without transverse reinforcement: from refined experimental measurements to mechanical models." PhD thesis. EPFL. 2017.
42. Tirassa M. "The transfer of forces through rough surface contact in concrete." PhD thesis. EPFL. 2020.
43. Schramm N, Fischer O, Scheufler W. Experimentelle Untersuchungen an vorgespannten Durchlauftrager Teilsystemen zum Einfluss nicht mehrzugelassener Bilgelformen auf die Querkrafttragfähigkeit. *Bauingenieur*. 2019;94.
44. Huber P. "Beurteilung der Querkrafttragfähigkeit bestehender Stahlbeton- und Spannbetonbrücken." PhD thesis. TU Wien. 2016.
45. Huber P, Huber T, Kollegger J. Investigation of the shear behavior of RC beams on the basis of measured crack kinematics. *Eng Struct*. 2016;113:41–58.
46. Tue NV, Ehmann R, Tung ND. Schubversuche an Stahlbetonbalken unterschiedlicher M/V-Kombinationen. *Beton- und Stahlbetonbau*. 2015;110(7):446–57.

AUTHOR BIOGRAPHIES



Sebastian Thoma, Chair of Concrete and Masonry Structures, Technical University of Munich, Munich, Germany.



Oliver Fischer, Chair of Concrete and Masonry Structures, Technical University of Munich, Munich, Germany.

How to cite this article: Thoma S, Fischer O. Experimental investigations on the shear strength of prestressed beam elements with a focus on the analysis of crack kinematics. *Structural Concrete*. 2023;24(4):4993–5010. <https://doi.org/10.1002/suco.202200699>